

1 Studies of uniformity of 50 μm low-gain avalanche detectors
2 at the Fermilab test beam.

3 A. Apresyan^{*,a}, S. Xie^b, C. Pena^b, R. Arcidiacono^{e,g}, N. Cartiglia^e, M. Carulla^h,
4 G. Derylo^a, M. Ferrero^e, D. Flores^h, P. Freeman^d, Z. Galloway^d, A. Ghassemiⁱ, H. Al
5 Ghoul^c, L. Gray^a, S. Hidalgo^h, S. Kamadaⁱ, S. Los^a, M. Mandurrino^e, A. Merlos^h,
6 N. Minafra^c, A. Ronzhin^a, G. Pellegrini^h, D. Quirion^h, C. Royon^c, H. Sadrozinski^d,
7 A. Seiden^d, V. Sola^e, M. Spiropulu^b, A. Staiano^e, L. Uplegger^a, K. Yamamotoⁱ,
8 K. Yamamuraⁱ

9 ^a*Fermi National Accelerator Laboratory, Batavia, IL, USA*

10 ^b*California Institute of Technology, Pasadena, CA, USA*

11 ^c*University of Kansas, KS, USA*

12 ^d*SCIPP, University of California Santa Cruz, CA, USA*

13 ^e*INFN, Torino, Italy*

14 ^f*Università di Torino, Torino, Italy*

15 ^g*Università del Piemonte Orientale, Italy*

16 ^h*Centro Nacional de Microelectrónica (IMB-CNM-CSIC), Barcelona, Spain*

17 ⁱ*Hamamatsu Photonics (HPK), Hamamatsu, Japan*

18 **Abstract**

In this paper we report measurements of the uniformity of time resolution, signal amplitude, and charged particle detection efficiency across the sensor surface of low-gain avalanche detectors (LGAD). Comparisons of the performance of sensors with different doping concentrations and different active thicknesses are presented, as well as their temperature dependance and radiation tolerance up to $6 \times 10^{14} \text{ n/cm}^2$. Results were obtained at the Fermilab test beam facility using 120 GeV proton beams, and a high precision pixel tracking detector. LGAD sensors manufactured by the Centro Nacional de Microelectrónica (CNM) and Hamamatsu Photonics (HPK) were studied. The uniformity of the sensor response in pulse height before irradiation was found to have a 2% spread. The signal detection efficiency and timing resolution in the sensitive areas before irradiation were found to be 100% and 30-40 ps, respectively. A “no-response” area between pads was measured to be about 70 μm for CNM and 110 μm for HPK sensors. After a neutron fluence of $6 \times 10^{14} \text{ n/cm}^2$ the CNM sensor exhibits a large gain variation of up to a factor of 2.5 when comparing metallized and non-metallized sensor areas. An irradiated CNM sensor achieved a time resolution of 30 ps for the metallized area and 40 ps for the non-metallized area, while a HPK sensor irradiated to the same fluence achieved a 30 ps time resolution.

19 *Key words:*

20 Silicon, Timing, LGAD, Test Beam

| | | | |
|-----------|-----------------|--|-----------|
| 21 | Contents | | |
| 22 | 1 | Introduction | 2 |
| 23 | 2 | Experimental Setup | 3 |
| 24 | 3 | LGAD Sensor Properties | 5 |
| 25 | 4 | Readout Electronics | 7 |
| 26 | 5 | Timestamp Reconstruction | 7 |
| 27 | 6 | Sensor Studies and Analysis | 9 |
| 28 | 6.1 | Study of the uniformity of the LGAD sensors | 9 |
| 29 | 6.2 | Measurement of the “no-response” area between two neighboring pixels . . | 12 |
| 30 | 6.3 | Comparison of HPK doping profiles | 13 |
| 31 | 6.4 | Comparison of uniformity of HPK 50 μm with 80 μm | 15 |
| 32 | 6.5 | Temperature dependence of the LGAD sensors | 15 |
| 33 | 6.6 | Radiation tolerance of the LGADs | 23 |
| 34 | 7 | Conclusion | 24 |

35 1. Introduction

36 Future colliders, including the high luminosity upgrade of the Large Hadron Collider
37 (HL-LHC) at CERN, will operate with an order of magnitude higher instantaneous lu-
38 minosity compared to what has been achieved at the large hadron collider (LHC) so
39 far. With the increased instantaneous luminosity, the rate of simultaneous interactions
40 per bunch crossing (pileup) is projected to reach an average of 140 to 200. The large
41 amount of pileup increases the difficulties in separating particles from the hard scatter-
42 ing interaction with those produced in different pileup interactions. In particular, the
43 ability to discriminate between jets produced in the events of interests, especially those
44 associated with vector boson fusion processes, and jets produced by pileup interactions
45 will be degraded. Additionally, the efficiency to identify high p_{T} isolated electrons and
46 muons will be severely reduced due to the high density of pileup particles in their vicinity.
47 The missing transverse energy resolution will also deteriorate, and several other physics
48 objects performance metrics will also suffer the detrimental effects of pileup.

49 One way to mitigate the pileup effects mentioned above, complementary to precision
50 tracking methods, is to perform a time of arrival measurement associated with each par-
51 ticle. Such a measurement with a precision of about 30-40 ps, will reduce the effective
52 amount of pileup by a factor of 10, given that the spread in collision time of the pileup
53 interactions at HL-LHC is foreseen to be approximately 200 ps. It has been previously
54 shown that a precision of better than 20 ps can be achieved for electromagnetic showers

*Corresponding author
Email address: apresyan@fnal.gov (A. Apresyan)

measured with silicon sampling calorimeters [1–3] using traditional planar silicon detectors. In this paper, we report results of particle beam measurements with thin low-gain avalanche detectors (LGAD) that have been shown to achieve time resolutions around 30 ps [4, 5]. LGAD are envisioned to be used in the CMS and ATLAS experiment upgrades for HL-LHC in order to overcome the event reconstruction challenges posed by the high rate of concurrent collisions per beam crossing. The implemented regions of pseudorapidity (η) are: $|\eta| > 1.5$, and $2.4 < |\eta| < 4.2$ for CMS and ATLAS, respectively. In order to achieve the desired timing precision across a large area of the detectors, the sensors will need to provide high uniformity of signal response and timing resolution. In this paper, we perform detailed measurements of the performance of LGAD sensors produced by Centro Nacional de Microelectrónica (CNM) and Hamamatsu Photonics (HPK) exposed to the 120 GeV proton beam at Fermilab. Utilizing high-precision tracking detectors we extract position dependence of the charged-particle detection efficiency, signal pulse height, signal timestamp, and time resolution of 50 μm LGAD sensors. We also compare the uniformity of 50 and 80 μm LGAD sensors. Uniformity and time resolution of the HPK and CNM sensors irradiated to an equivalent neutron fluence of $6 \times 10^{14} \text{ n/cm}^2$ are also presented. Detailed measurements of irradiated HPK sensors were presented in Ref. [6].

The paper is organized as follows: the experimental setup is described in Sec. 2; the tested LGAD sensors and their operating conditions are listed in Sec. 3; readout electronics used in the measurements are described in Sec. 4; algorithms used in the event reconstruction are described in Sec. 5; beam test results are presented in Sec. 6, followed by the conclusion in Sec. 7.

2. Experimental Setup

Test-beam measurements were performed at the Fermilab Test-beam Facility (FTBF) which provided a 120 GeV proton beam from the Fermilab Main Injector accelerator. The Devices Under Test (DUTs) were mounted on a remotely operated motorized stage, placed inside the pixel telescope detector [7]. The latter provides better than 10 μm position resolution for charged particles impinging on the DUT. Additionally, a Photek 240 micro-channel plate (MCP-PMT) detector [8–11] was placed furthest downstream, and provided a very precise reference timestamp. Its precision has been previously measured to be less than 7 ps [10]. A schematic diagram and photograph of the experimental area are shown in Fig. 1 and Fig. 2, respectively.

The DAQ system for the DUTs and the Photek MCP-PMT is based on a CAEN V1742 digitizer board [12], which provides digitized waveforms sampled at 5 GS/s, and with one ADC count corresponding to 0.25 mV. The CAEN digitizer was voltage- and time-calibrated using the procedure described in Ref. [13]. One of the main parameters of DAQ system for precise time measurements is the “electronic time resolution”, defined as the measured time jitter between two signals that are split from the same source. These two signals are used as “start” and “stop” signals to electronic system measuring the time interval between them. The electronic time resolution of the CAEN V1742 digitizer was measured to be less than 4 ps, and thus, its impact on the timing measurements presented in these studies can be neglected. The DAQ for the pixel telescope is based on the CAPTAN system developed at Fermilab [7]. The track-reconstruction is performed using the Monicelli software package developed specifically for the test-beam application.

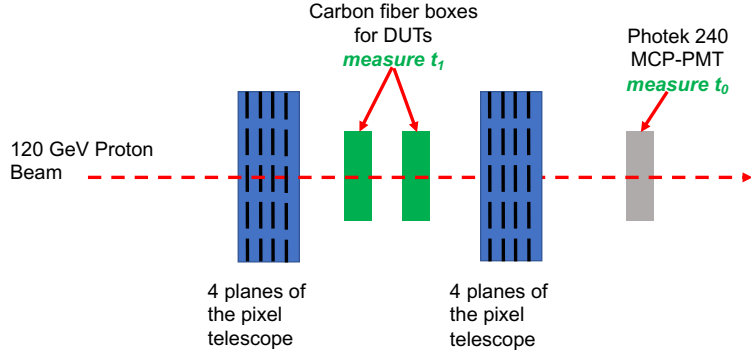


Figure 1: A schematic diagram of the test-beam setup is shown. The t_0 and t_1 are defined in Section 4.

100 The DUTs were placed inside the telescope box described in Ref.[7], and mounted on
 101 an aluminum mechanical support structure. The telescope box can be moved remotely
 102 in both the horizontal and vertical directions in order to align the DUTs with the beam.
 103 The aluminum support structure for the DUTs provide both mechanical stability and
 104 are equipped with Peltier cooling elements that were used in this study to operate the
 105 DUTs at -10° and -20° C.

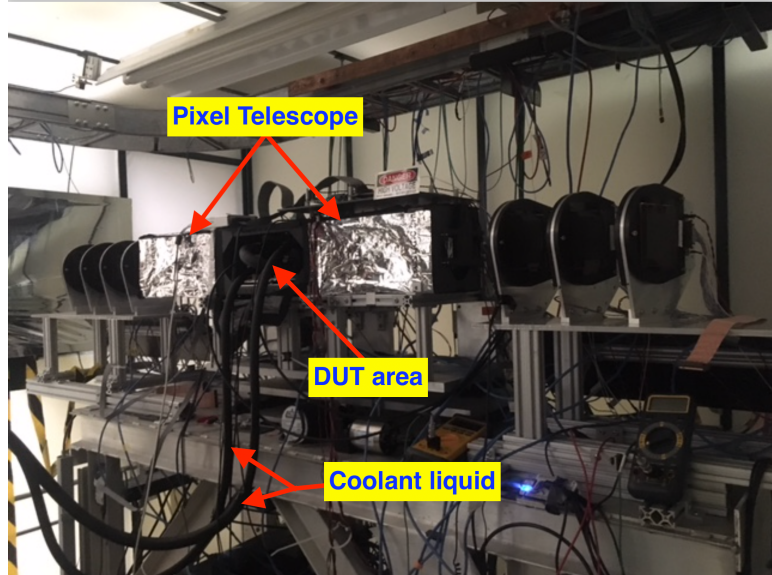


Figure 2: A picture of the experimental area. Thea pixel telescope detectors are placed inside the electrostatic-discharge shielded boxes on the two sides of the DUT area. Cooling liquid for the Peltier elements inside the DUT area is provided by the two tubes shown in the picture.

106 The beam is resonantly extracted in a slow spill for each Main Injector cycle delivering
 107 a single 4.2 sec long spill per minute. The primary beam (bunched at 53 MHz) consists

108 of 120 GeV protons. All measurements presented in this paper were taken with the
 109 primary beam particles. The trigger to both the CAEN V1742 and to the pixel telescope
 110 was provided by a scintillator mounted on a photomultiplier tube, placed upstream of
 111 the DUTs in the beam-line. Due to the limited buffer depth of the CAEN V1742 board,
 112 special care had to be taken in the design of the DAQ system to ensure that both the DUT
 113 and telescope DAQs collect exactly the same amount of triggers. This was achieved by
 114 limiting the trigger rate by introducing an adjustable dead-time using a custom-designed
 115 trigger board. Processed data from the pixel telescope and the DUTs were merged offline
 116 by matching the trigger counters recorded by the two systems.

117 3. LGAD Sensor Properties

118 Sensors manufactured by HPK and CNM were measured in the test beam experiment.
 119 Both single- and four-channel configurations of the sensor were used in the measurements.
 120 The sensors studied have active thicknesses of about 50 μm and 80 μm . A brief summary
 121 of the sensors dimensions and capacitances is presented in Tab. 1.

122 CNM sensors have an active thickness of about 45 μm and were produced on 4-inch
 123 Silicon-on-Insulator wafers with a 45 μm thick high resistivity float zone (FZ) active layer
 124 on top of a 1 μm buried oxide and a 300 μm support wafer. The back-side contact is
 125 achieved through wet-etched deep access holes through the insulator. The dose of the
 126 boron implantation for the W9HG11 sensor is 1.9×10^{13} atoms/cm $^{-2}$, and 2.0×10^{13}
 127 atoms/cm $^{-2}$ for the W11LGA35. Details on CNM sensors can be found in Ref. [4, 14].

128 The HPK sensors were manufactured on 6-inch silicon wafers of 150 μm total thickness
 129 with a 50 μm or 80 μm thick high resistivity float zone (FZ) active layer. Four gain splits,
 130 identified with the letters A (lowest gain) to D (highest gain), were produced identical
 131 in the mask design but with a different p^+ dose of the gain layer to study the optimal
 132 parameters for fast timing detectors. The pads were produced in three versions: two with
 133 guard ring (GR and GBGR) and one without guard ring. Four-channel sensors in a 2×2
 134 array were produced with all 4 gain-splits, and are identified with the PIX identifier. For
 135 example, the 2×2 array of the 50 μm sensor split D is labelled as 50D-PIX. The sensor
 136 corresponding to each of the four channels in the array is also referred to as a pixel in
 137 this paper. Each pixel in the 2×2 HPK array has dimensions of $3 \times 3 \text{ mm}^2$. The CNM
 138 single-channel sensors are square pads with an active area of 1.7 mm^2 while the HPK
 139 single-channel sensors are circular pads with an active area of 0.8 mm^2 .

| Sensor | Number of channels | Single channel dimensions | Single channel capacitance |
|--------------|--------------------|--------------------------------|----------------------------|
| HPK 50A-PIX | 4 | $3 \times 3 \text{ mm}^2$ | 20 pF |
| HPK 50B-PIX | 4 | $3 \times 3 \text{ mm}^2$ | 20 pF |
| HPK 50C-PIX | 4 | $3 \times 3 \text{ mm}^2$ | 20 pF |
| HPK 50D-PIX | 4 | $3 \times 3 \text{ mm}^2$ | 20 pF |
| HPK 80C-PIX | 4 | $3 \times 3 \text{ mm}^2$ | 12 pF |
| HPK 50D | 1 | $\varnothing = 1.0 \text{ mm}$ | 2.9 pF |
| CNM-W9HG11 | 4 | $3 \times 3 \text{ mm}^2$ | 22 pF |
| CNM-W11LGA35 | 1 | $1.3 \times 1.3 \text{ mm}^2$ | 3.9 pF |

Table 1: Linear dimensions and capacitances of the sensors used in these studies.

140 The list of sensors studied in this article, as well as the temperature and the sensor
 141 bias voltage used during their operation are listed in Tab. 2.

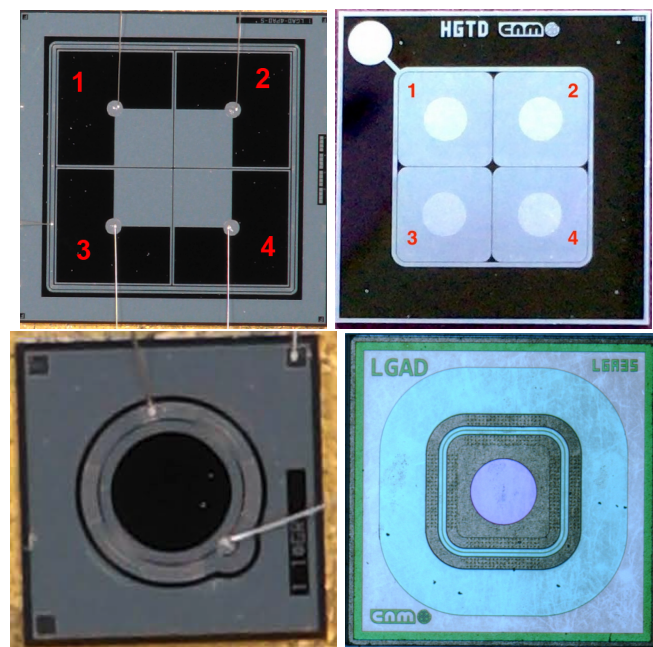


Figure 3: Photographs of the HPK 50D-PIX 2×2 array sensor (top left), the CNM W9HG11 2×2 array sensor (top right), the HPK 50D-GR single sensor (bottom left), and the CNM W11LGA35 single sensor (bottom right) are shown. Numerical labels overlaid on top of the images of the array sensors are used in the text when referring to individual pixels.

| Sensor | KU Board 2-ch | UCSC board 4-ch | FNAL board 4-ch |
|---|--------------------|--------------------|--|
| HPK 50A-PIX | -630 V (20) | — | — |
| HPK 50B-PIX | -550 V (25) | — | — |
| HPK 50C-PIX | -400 V (20) | -450 V (35) | — |
| HPK 50D-PIX | -300 V (30) | — | -250 V (17), -300 V (30), -250 V (29) -250 V (36) |
| CNM W9HG11 $6 \times 10^{14} \text{ n/cm}^2$ | — | -180 V (14) | — |
| CNM W11LGA35 $6 \times 10^{14} \text{ n/cm}^2$ | — | — | -400 V (24), -420 V (28) |

Table 2: Data taking conditions for the studies presented in this paper. Numbers in bold indicate that the sensor was at room temperature, underlined ones were taken at -10C° , and those in italicized text were taken at -20C° .

142 4. Readout Electronics

143 Three readout electronics boards were used in various measurements presented in this
 144 paper. They were independently developed at Fermi National Accelerator Laboratory
 145 (FNAL), at the University of Kansas (KU), and at the University of California Santa
 146 Cruz (UCSC).

147 The 4-channel Fermilab LGAD test board is designed to test sensors up to 8.5 mm
 148 by 8.5 mm at voltages up to 1 kV. Four wire-bonding pads allow for signal readout
 149 via amplifiers based on Mini-Circuits GALI-66+. The amplifiers feature transformers
 150 with 1:2 input impedance matching, two stages of amplification and a 500 MHz low-
 151 pass filter. In this full configuration, the amplifiers feature 12.5Ω input impedance, $5 \text{ k}\Omega$
 152 transimpedance, 500 MHz bandwidth and 1 mV rms output noise. If needed it is possible
 153 to jump the input transformer and/or the low-pass filter, which would result in an input
 154 impedance of 50Ω , transimpedance of $10 \text{ k}\Omega$, and bandwidth of 2 GHz.

155 The 2-channel KU board, designed and produced by the University of Kansas, can
 156 accommodate many types of sensors including diamond, silicon, LGAD or avalanche
 157 photodiodes (APD). The sensor is hosted on the board itself and the electronics was
 158 optimized for precise timing measurements. In particular, the amplifier, made with
 159 discrete components, has an input impedance of 700Ω , an output noise of 4 mV and a
 160 gain in transresistance of about $50 \text{ mV}/\mu\text{A}$ with a 3 dB bandwidth of 100 MHz. Those
 161 values were simulated for an input capacitance of 20 pF, which corresponds roughly to
 162 an LGAD of 9 mm^2 . The power consumption of the board is about 130 mW per channel.

163 The UCSC 1-channel board is described in detail in Ref. [4]. This board uses discrete
 164 components and contains several features which allow for maintaining a wide bandwidth
 165 ($\sim 2 \text{ GHz}$) and a low noise even in noisy environments. The inverting amplifier uses a
 166 high-speed SiGe transistor which has a transimpedance of about 470Ω . A commercial
 167 inverting amplifier with gain 10x is used to boost the signal. The 4-channel UCSC board
 168 has two stages: the first one is identical to the UCSC single channel board, and is followed
 169 by an inverting stage. The total transimpedance is $10.7 \text{ k}\Omega$.

170 5. Timestamp Reconstruction

171 As discussed in Section 2, the reference time is measured using the Photek MCP-
 172 PMT detector. The timestamp for this reference detector is obtained by fitting the peak

173 region of the pulse to a Gaussian function and the mean parameter of the Gaussian is
 174 assigned as the timestamp t_0 . A more detailed description can be found in Ref [8].

175 The timestamp for signals from the LGAD sensors is obtained in two different ways
 176 depending on which read-out board was used. For the FNAL and UCSC boards, whose
 177 pulse widths are less than 2 ns, the timestamp is obtained via a fit to a Gaussian function
 178 analogous to what is done for the reference detector. For the KU board, whose pulses
 179 take much longer to fall to the baseline, the timestamp is obtained by performing a linear
 180 fit to the rising edge of the pulse, between 15% and 70% of the maximum amplitude, and
 181 the time at which the pulse reaches 45% of the maximum amplitude is assigned as its
 182 timestamp t_1 . We refer to this algorithm as the constant fraction discriminator (CFD)
 183 method. This procedure is slightly different compared to previous studies of LGAD
 184 sensors, where the CFD method was used uniformly.

185 The choices of the timestamp reconstruction algorithms listed above were motivated
 186 by the result of a dedicated study of various algorithms for each of the three readout
 187 boards. The study is performed using signals from the HPK 50D sensor. Constant
 188 fraction discriminant (CFD) and constant threshold discriminant (CTD) algorithms are
 189 used and the time resolution performance is studied as a function of the threshold used. In
 190 Tables 3 and 4, we show the time resolution obtained for different thresholds for the CFD
 191 and CTD algorithms respectively, for the KU readout board. For the CFD algorithm, we
 192 observed no significant dependence of the timestamp on the pulse height of the signal.
 193 However, for the CTD algorithm, the timestamp does depend on the pulse height and
 194 requires a correction referred to as a time-walk correction. For most situations, the time-
 195 walk correction can be accurately described by a linear dependence of timestamp on
 196 pulse height, however we do observe that as the CTD threshold increases, the time-walk
 197 correction becomes more quadratic. In Table 4, the time resolution is reported for both
 198 linear and quadratic time-walk corrections. We observe that the best results are obtained
 199 for a CFD threshold at 45%. However the CTD algorithm at a moderate threshold does
 200 yield comparable time resolutions.

| CFD Threshold | Time Resolution |
|---------------|-----------------|
| 15% | 45 ps |
| 30% | 40 ps |
| 45% | 38 ps |
| 60% | 39 ps |

Table 3: Time resolution measured for the HPK 50D-PIX sensor on the KU readout board using the constant fraction discriminant algorithm.

| CTD Threshold | Time Resolution (Linear Time-walk Correction) | Time Resolution (Quadratic Time-walk Correction) |
|---------------|--|---|
| 12 mV | 52 ps | 51 ps |
| 18 mV | 46 ps | 45 ps |
| 24 mV | 43 ps | 42 ps |
| 37 mV | 41 ps | 40 ps |
| 49 mV | 43 ps | 39 ps |
| 61 mV | 43 ps | 39 ps |
| 73 mV | 45 ps | 40 ps |

Table 4: Time resolution measured for the HPK 50D-PIX sensor on the KU readout board using the constant threshold discriminant algorithm.

201 In Table 5, we show the analogous study performed for the FNAL and UCSC readout
 202 boards. As signals on these readout boards have fast decay times, the Gaussian fit yields
 203 the best performance. As for the KU readout board, the CFD and CTD algorithms again
 204 give similar performance for the FNAL and UCSC readout boards.

| Timestamp Algorithm Type | Time Resolution (FNAL Board with (HPK 50D-PIX Sensor) | Time Resolution (UCSC Board with irradiated HPK 50D Sensor) |
|--|---|---|
| Gaussian Fit | 42 ps | 35 ps |
| CFD at 15% Threshold | 71 ps | 47 ps |
| CFD at 30% Threshold | 60 ps | 42 ps |
| CFD at 45% Threshold | 53 ps | 39 ps |
| CFD at 60% Threshold | 56 ps | 44 ps |
| CTD at 18 mV Threshold (Linear Time-walk Correction) | 55 ps | 43 ps |
| CTD at 18 mV Threshold (Quadratic Timewalk Correction) | 52 ps | 37 ps |

Table 5: Time resolution measured for the HPK 50D-PIX sensor on the FNAL readout board and the irradiated HPK 50D sensor on the UCSC board for a variety of timestamp reconstruction algorithms.

205 6. Sensor Studies and Analysis

206 We present a number of different studies performed on the LGAD sensors described
 207 in Section 3. They include signal response uniformity, gap distance between adjacent
 208 pixels, doping profile and sensor thickness characterization, temperature and irradiation
 209 dependence, and time resolution. A brief overview of the analysis methods is given below,
 210 followed by subsections describing the details and results of each study.

211 Events are required to have a signal in the Photek MCP-PMT consistent with a
 212 minimum ionizing particle (MIP), and a signal above the noise in LGAD sensors. The
 213 signal selection in the Photek MCP-PMT is the same for all runs and requires that the
 214 signal is consistent with a MIP corresponding to amplitude values in the range between
 215 160 mV and 320 mV. Signal events in LGAD sensors are selected such that they are
 216 above the noise levels listed for each board in Sec. 4. All measurements other than those
 217 described in Sec. 6.5 and 6.6 were performed at room temperature.

218 Here, and in the remainder of this article, whenever a scan of a certain characteristic
 219 quantity – e.g. time resolution – of the sensor is presented, we show the X-axis scan for
 220 pixels 1 and 2, and the Y-axis scan for pixels 1 and 3, as defined on the left picture in
 221 Fig. 3. The X-axis scan across pixels 3 and 4, and Y-axis scan across pixels 2 and 4 show
 222 qualitatively the same features, and are not presented here. Measurements presented
 223 for various sensors were obtained from different datasets and therefore the statistical
 224 precision is not always the same. The reason that in some measurements the error bars
 225 are not the same across either X- or Y-coordinate is due to the fact that the beam does
 226 not uniformly illuminate the whole sensor area, and hence the number of events is not
 227 the same across sensor surface.

228 6.1. Study of the uniformity of the LGAD sensors

229 We present in detail uniformity studies – including signal detection efficiency, most
 230 probable value, time difference, and time resolution – across the sensitive area of the

231 LGAD. The sensors under study were produced by HPK and CNM. The largest dataset
 232 was collected for the HPK 50D-PIX and the CNM W9HG11 sensors. The HPK 50D-PIX
 233 sensor was mounted on the 4-channel FNAL board and biased to -300 V, while the CNM
 234 W9HG11 sensor was mounted on the 4-channel UCSC board and biased to -180 V. Both
 235 sensors were operated at room temperature for these studies.

236 The measurements of the particle detection efficiency are shown in Fig. 4. Efficiency
 237 is defined as the ratio of events that register a signal above the noise level to those that
 238 contain a track identified by the pixel telescope pointing at the LGAD sensor. Error bars
 239 in all efficiency measurements are evaluated as Clopper-Pearson intervals for calculating
 240 binomial confidence intervals. Noise values for different boards used in the experiments
 241 are listed in Sec. 4, and were measured using dedicated runs with no particles, and
 242 data collected using random triggers. Signals used in the efficiency measurements were
 243 required to have amplitude above 20 mV plots, well above the noise level.

244 We observe a flat 100% efficiency across the whole sensor area. The left edge in the
 245 X-axis scan of pixel 1 on HPK 50D-PIX sensor in Fig. 4 is outside the acceptance of the
 246 pixel telescope, hence the efficiency curve does not fully cover its surface. A clear drop
 247 in efficiency is observed in the transition (“no-response”) region between the two pixels.
 248 A more detailed study of the “no-response” region is given in Sec. 6.2.

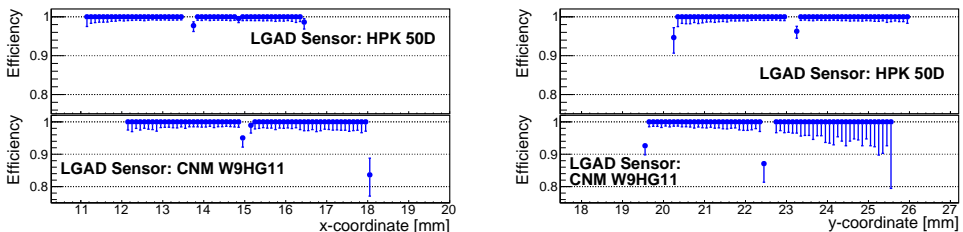


Figure 4: Efficiency measurement across the X-axis (left) and Y-axes (right) of the HPK 50D-PIX sensor mounted on the FNAL board, and the CNM W9HG11 sensor mounted on the UCSC board. The scans of pixels 1 and 2 along the X-axis, and pixels 1 and 3 along the Y-axis are shown. The pixel numbering scheme is defined in Fig. 3.

249 An important characteristic is the uniformity of the signal size across the surface of the
 250 sensor, which directly impacts on its timing performance. We use the signal amplitude
 251 as the metric to characterize the signal size uniformity. The distribution of the LGAD
 252 signal amplitudes is fitted to a Landau distribution. An example of the fit is shown in
 253 Fig. 5. The most probable value (MPV) parameter of the fitted Landau distribution is
 254 plotted in Fig. 6. A flat response with a uniform signal size is observed over the whole
 255 sensor area. As a study of systematic effects, we have also repeated the fit using the
 256 convolution of a Landau function and a Gaussian function to model the impact of noise
 257 and fluctuations in the multiplication process. We find that the peak location increases
 258 systematically by about 5% for all points in a correlated fashion. However it does not
 259 appear to impact the conclusions drawn on the response uniformity.

260 The measurements of the time difference $\Delta t = t_1 - t_0$ between the reference timestamp
 261 (t_0) and the timestamp of the LGAD sensors (t_1) are shown in Fig. 7. The micro-bonding
 262 scheme of the HPK and CNM 2×2 sensor arrays is shown in Fig. 3. For the HPK sensor,
 263 the Δt dependence on the hit position indicates a shift of about 20–30 ps between the

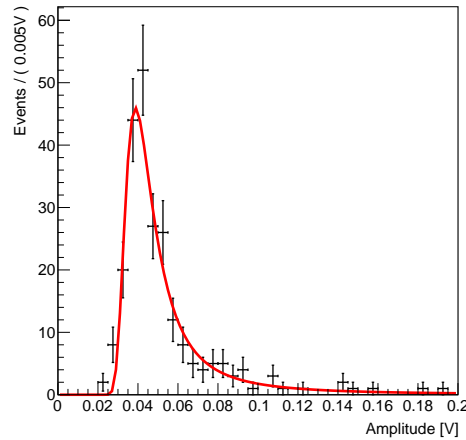


Figure 5: The signal amplitude distribution is fitted to a Landau function. The data corresponds to one bin of the X-axis scan.

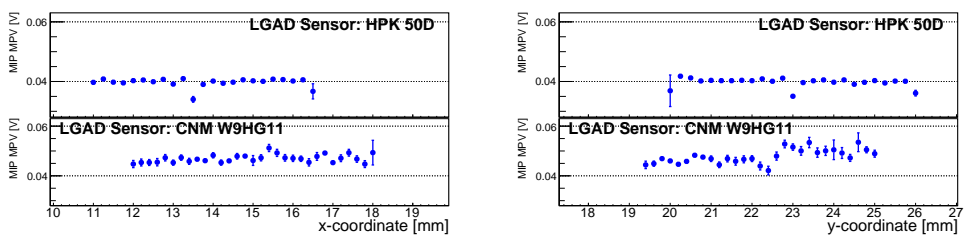


Figure 6: Signal amplitude MPV measurement across the X-axis (left) and Y-axes (right) of the HPK 50D-PIX sensor mounted on the FNAL board, and the CNM W9HG11 sensor mounted on the UCSC board. The scans of pixels 1 and 2 along the X-axis and pixels 1 and 3 along the Y-axis are shown. The pixel numbering scheme is defined in Fig. 3.

264 metallized area near the center of the array (gray region of the top-left image in Fig. 3)
 265 and the non-metallized area. This effect cannot be attributed to the algorithm used
 266 to time-stamp the events, since the same behavior is observed with the CFD and CDT
 267 algorithms. Furthermore, the same behavior is observed on all HPK sensor varieties
 268 mounted on KU board, as presented in Sec. 6.3. The CNM W9HG11 sensor does not
 269 contain metallized areas on its surface and we do not observe the same effect. Further
 270 studies are needed to understand the effect.

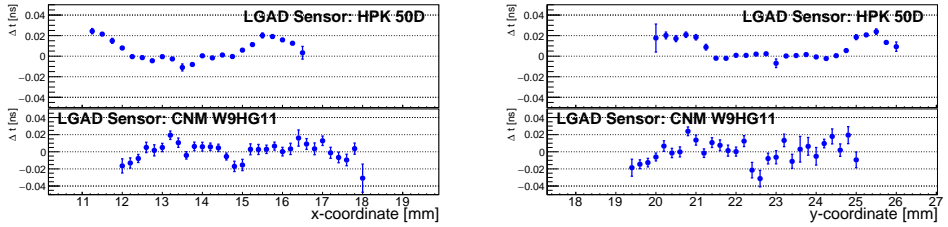


Figure 7: Δt measurement across the X- and Y-axes of the HPK 50D-PIX sensor mounted on the FNAL board, and the CNM W9HG11 sensor mounted on the UCSC board. The scans of pixels 1 and 2 along the X-axis, and pixels 1 and 3 along the Y-axis are shown. The pixel numbering scheme is defined in Fig. 3.

271 The measurement of the time resolution across the sensor surface is shown in Fig. 8.
 272 The distribution of Δt between the timestamp of the LGAD signal and the reference
 273 signal is fitted with a Gaussian function, and the spread σ of the fitted function is
 274 defined as the time resolution. We observe a uniform time resolution around 40 ps across
 275 the whole surface area for HPK, and around 55 ps for CNM sensors.

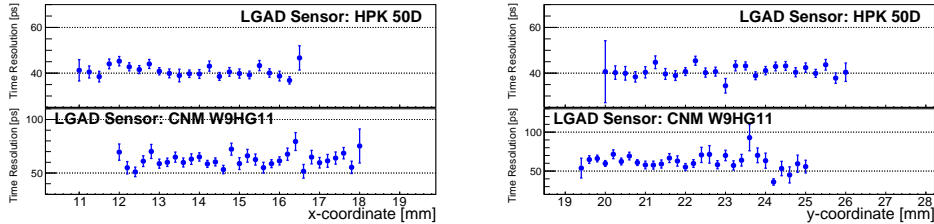


Figure 8: Time resolution measurement across the X-axis (left) and Y-axes (right) of the HPK 50D-PIX sensor mounted on the FNAL board, and the CNM W9HG11 sensor mounted on the UCSC board. The scans of pixels 1 and 2 along the X-axis, and pixels 1 and 3 along the Y-axis are shown. The pixel numbering scheme is defined in Fig. 3.

276 6.2. Measurement of the “no-response” area between two neighboring pixels

277 In order to precisely measure the width of the no-response area between two neigh-
 278 boring pixels, a large statistics sample of about 350,000 events was collected with the
 279 HPK 50D-PIX sensor mounted on a 2-channel KU board. The sensor was biased to
 280 -300 V. The large dataset allowed us to perform a detailed scan in the area between
 281 the two pixels as shown in Fig. 9. In order to estimate the width of the no-response
 282 between the pixels, the efficiency curves of the two neighboring pixels are fitted with an

283 S-curve function of the form $y = p_1 \times \text{Erf}\{\pm(p_2 - x)/p_3\} + p_4$, where $\text{Erf}\{x\}$ is the error
 284 function defined as:

$$\text{Erf}(x) = \frac{2}{\sqrt{\pi}} \times \int_0^x e^{-t^2} dt \quad (1)$$

285 , and p_i were free parameters of the fit. We define the width of the “no-response” area as
 286 the distance between the half-maxima of the two fitted S-curves, as shown in Fig. 9. We
 287 measure the width of the no-response area on the HPK 50D-PIX sensor to be $110 \mu\text{m}$,
 288 with an uncertainty of $10 \mu\text{m}$. Data points outside the sensor area in Figs. 9, 10 actually
 289 had hit the sensor active area, but the coordinate of the track is incorrectly assigned,
 290 due to a small probability ($< 1\%$) to misreconstruct the position of the track.

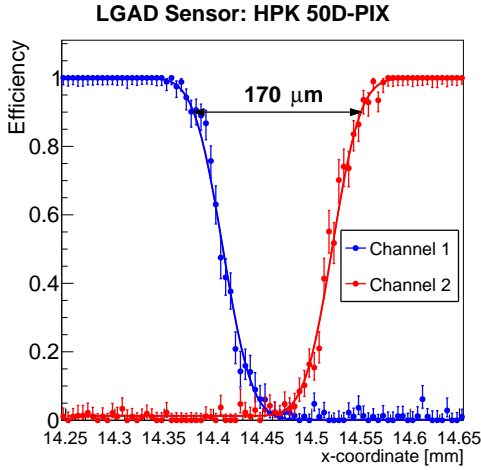


Figure 9: A zoom-in version of the efficiency measurement as a function of the X position of the beam particle. The HPK 50D-PIX sensor was operated at -300 V bias voltage. The pixel numbering scheme is defined in Fig. 3.

291 A further measurement was made on the 4-channel UCSC board for the HPK 50C-
 292 PIX sensor and the CNM W9HG11 sensor. We compare the width of the gap region of
 293 the HPK and CNM sensors in Fig. 10. Both sensors in this comparison were tested in
 294 the beam simultaneously. The HPK 50C-PIX sensor was operated at -450 V , and CNM
 295 W9HG11 sensor was operated at -180 V . We measure the size of the “no-response”
 296 region to be around $110 \mu\text{m}$ on the HPK 50C-PIX – compatible with the HPK 50D-PIX
 297 sensor – and around $70 \mu\text{m}$ for the CNM sensor. Both measurements have an uncertainty
 298 of $10 \mu\text{m}$.

299 6.3. Comparison of HPK doping profiles

300 Studies of the dependence of the sensors’ characteristics on the doping concentrations
 301 were performed by comparing the $50 \mu\text{m}$ HPK PIX sensors of different gain splits.
 302 In order to reduce the impact of the variations between different readout boards, all
 303 measurements presented in this section were performed using only 2-channel KU readout
 304 boards. Four readout boards were prepared, each with an HPK sensor mounted on it, and

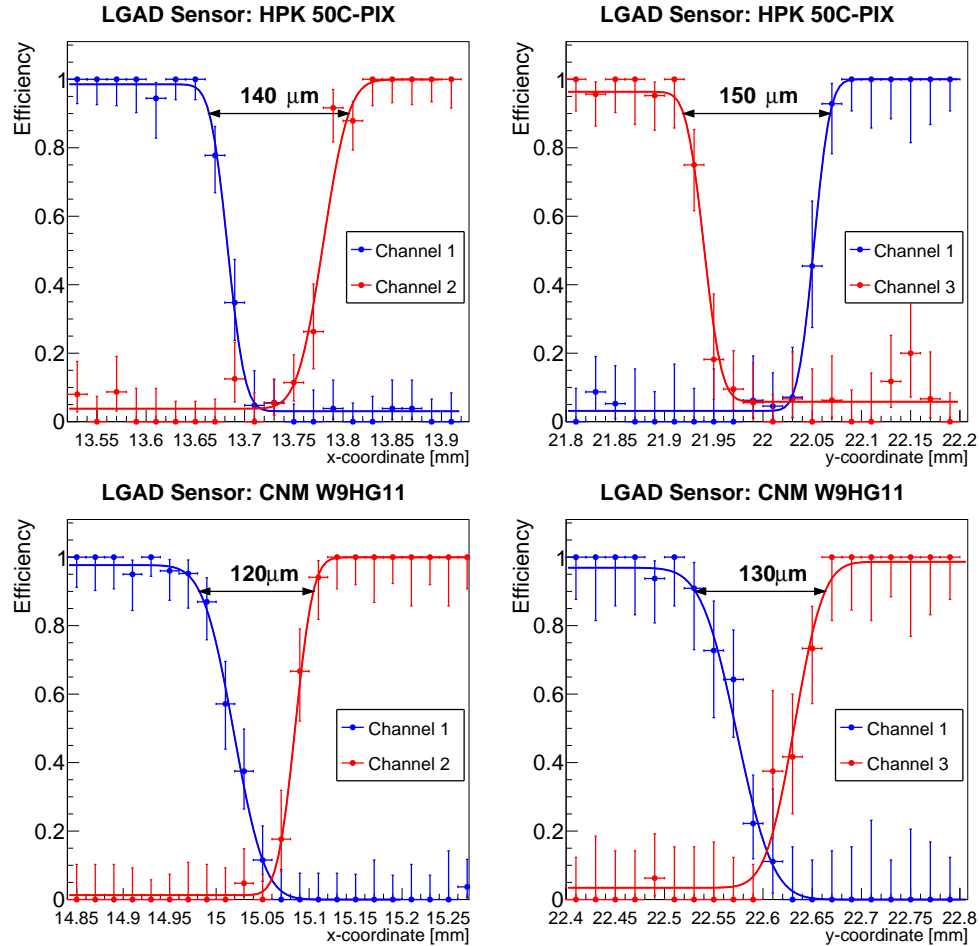


Figure 10: A zoom-in version of the efficiency measurement across the X- and Y-axes of the HPK 50C-PIX (top) and CNM W9HG11 (bottom) sensors. HPK sensor is operated at -450 V, and CNM sensor is operated at -180 V. Data points in blue are those from one pixel, and data points in red are from the neighboring pixel. The blue and red curves are fitted to the data points as described in the text. Arrows indicate the distance between the half-maximum points of the fitted curves.

305 tested in the beam. Data taken with the HPK 50D-PIX is the same as that presented
306 in Fig. 9, which is the largest data sample collected during this test beam campaign.
307 Therefore, the statistical uncertainties in the measurements of the HPK 50A-, B-, and
308 C-PIX sensors are larger than those of 50D-PIX. For this study, the sensors were oper-
309 ated at room temperature, and their bias voltages were set to -630 V, -550 V, -400 V,
310 and -300 V for the HPK 50A-PIX, HPK 50B-PIX, HPK 50C-PIX, and HPK 50D-PIX
311 sensors, respectively.

312 The distribution of the MPV of signal amplitudes across the sensor area is shown
313 in Fig. 11, where the MPV is extracted as described in Sec. 6.1. Comparing the signal
314 amplitudes between the two pixels we observe that the average amplitude varies between
315 the two channels. However, in Fig. 6 we observed that the amplitudes in the two pixels
316 of the same HPK 50D-PIX sensor on the FNAL readout board do not show the same
317 variations. We conclude that the observed difference in amplitude is due to imperfec-
318 tions in the manufacturing process of the custom-designed pre-amplifiers used in the KU
319 readout board and not due to sensor properties. Nevertheless, the signal MPV within a
320 single pixel is highly uniform for all tested samples.

321 The measurements of the time difference between the reference timestamp and the
322 timestamps of the HPK sensors are shown in Fig. 12. As was shown in Fig. 7, the Δt
323 exhibits an offset of about 20 ps between the metallized area and the non-metallized area
324 of the sensor. The feature is present in all 4 types of the HPK PIX sensors, does not
325 depend on the readout board or timestamp reconstruction algorithm used, and appears
326 to be statistically consistent in shape and magnitude.

327 The measurements of the time resolution across the sensors are shown in Fig. 13. We
328 observe a uniform time resolution around 40 ps across the entire sensor area.

329 6.4. Comparison of uniformity of HPK $50\ \mu\text{m}$ with $80\ \mu\text{m}$

330 The thickness of the active area of the sensor is an important design parameter when
331 optimizing for time resolution. A detailed study of time resolution of HPK sensors of 80
332 and $50\ \mu\text{m}$ is presented in [6]. Here we compare the uniformity of the time resolution
333 across the sensors of these two thicknesses. This study is performed using the HPK
334 C-PIX sensors with the same dopant concentration. The $80\ \mu\text{m}$ sensor HPK 80C-PIX
335 is biased at -610 V, while the $50\ \mu\text{m}$ sensor HPK 50C-PIX is biased at -400 V. The
336 sensors's gains at these bias voltages are: about 11 for the $80\ \mu\text{m}$ sensor, and about 14
337 for the $50\ \mu\text{m}$ sensor. The time resolution for the two sensors are shown in Fig. 14 as
338 a function of position, and exhibit fairly uniform behavior. Measurements of the HPK
339 50C-PIX sensor were performed on the KU 2-channel board, and those for HPK 80C-PIX
340 used the FNAL 4-channel board.

341 6.5. Temperature dependence of the LGAD sensors

342 In order to maintain their optimal performance at the highest fluences envisioned at
343 the HL-LHC, the LGAD sensors will be cooled to temperatures below -20°C degrees.
344 Operation at such low temperatures will allow to significantly reduce the leakage current.
345 The sensors yield higher gain at lower temperatures, but at the cost of a lower breakdown
346 voltage. Therefore, it is important to study the impact of the temperature on the gain and
347 time resolution, as well as their uniformity. In this section we describe the measurements
348 of the LGAD sensors performed at -10 and -20°C degrees, and compare the results to

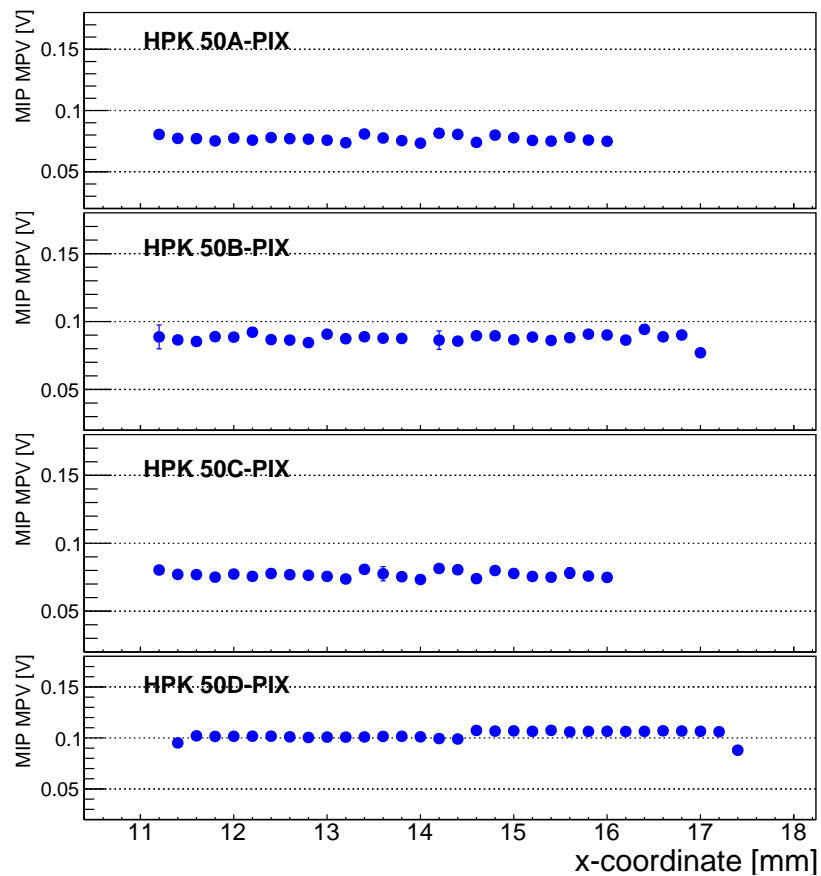


Figure 11: Signal amplitude MPV measurement across the X-axis of the HPK 50A-, 50B-, 50C-, and 50D-PIX sensors mounted on the KU board. The scan of pixels 1 and 2 along the X-axis, and pixel numbering scheme is defined in Fig. 3.

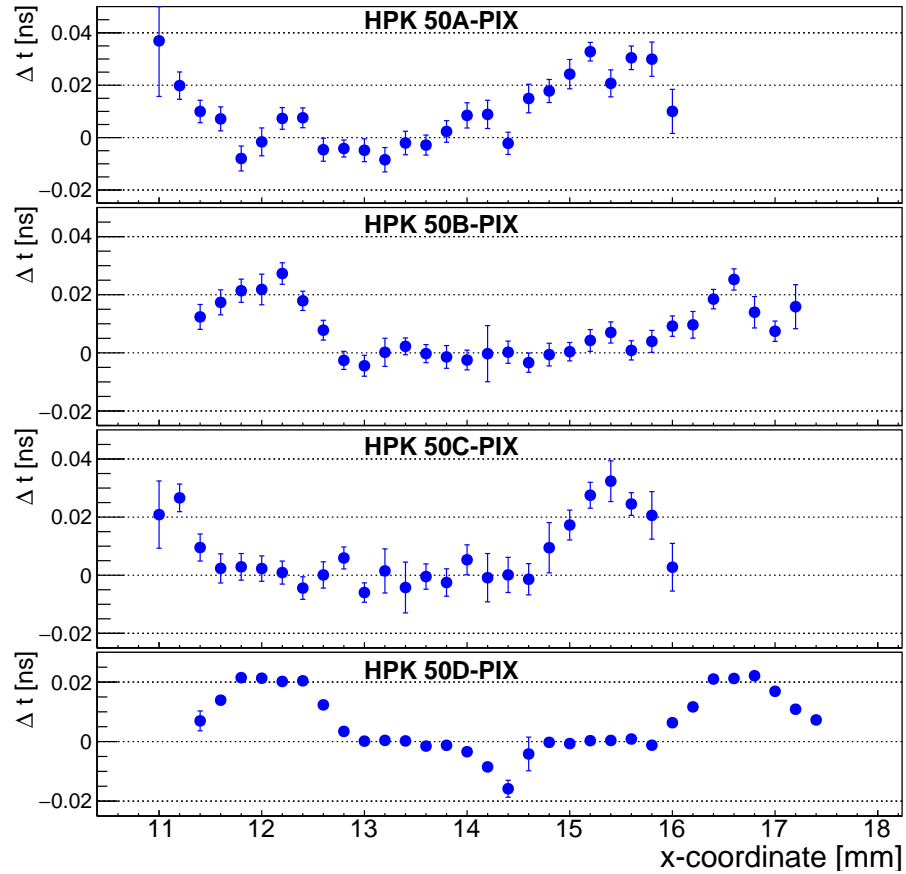


Figure 12: Δt measurements as a function of the X position of the beam particle for the HPK 50A-, 50B-, 50C-, and 50D-PIX sensors mounted on the KU board. The scan of pixels 1 and 2 along the X-axis is shown. The pixel numbering scheme is defined in Fig. 3.

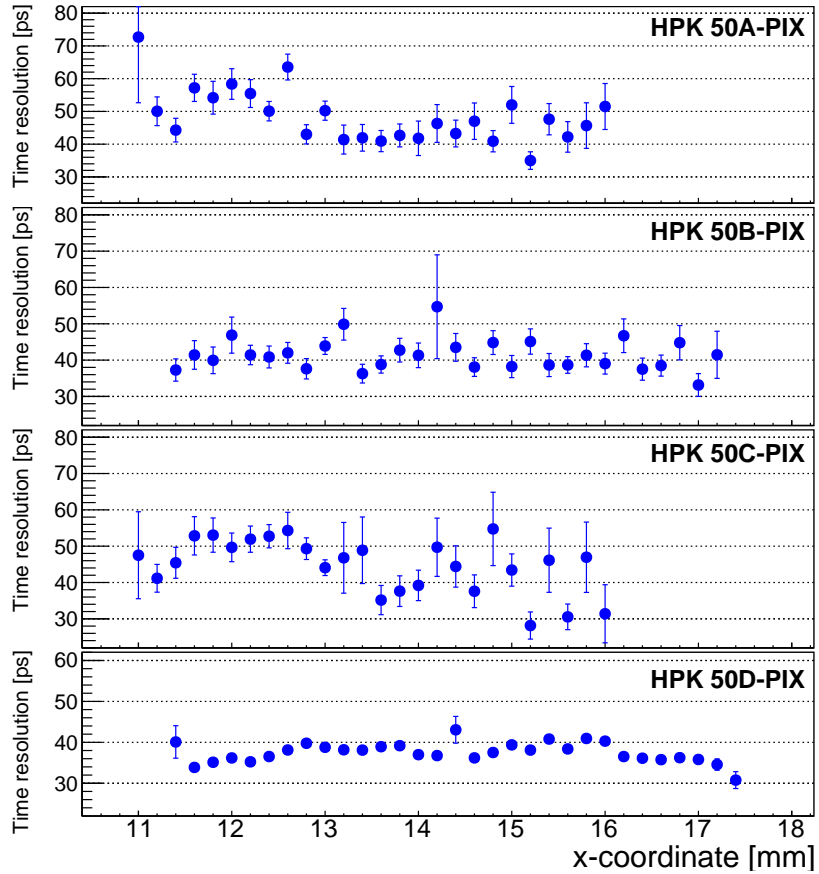


Figure 13: Time resolution measurements as a function of the X position of the beam particle for the HPK 50A-, 50B-, 50C-, and 50D-PIX sensors mounted on the KU board. The scan of pixels 1 and 2 along the X-axis is shown. The pixel numbering scheme is defined in Fig. 3.

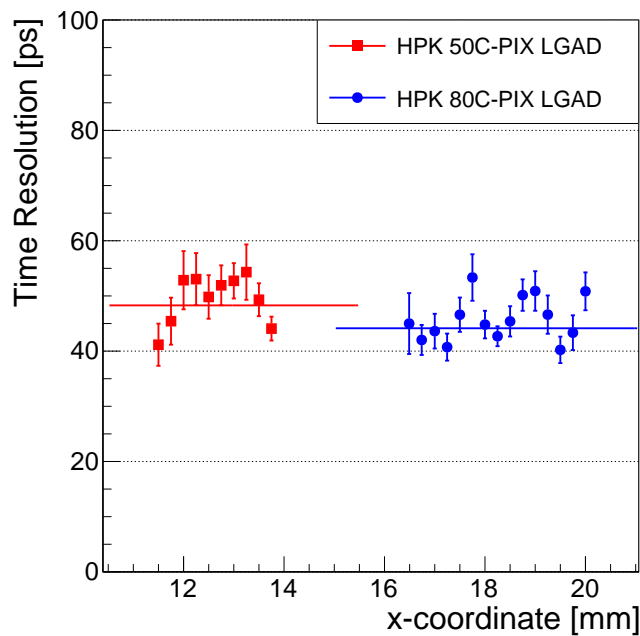


Figure 14: Comparison of the uniformity of the measured time resolution of the HPK 80C-PIX versus 50C-PIX sensors. The 80 μm sensor is mounted on the FNAL board, and is biased at -610 V, and the 50 μm sensor is mounted on the KU board and is biased at -400 V. The lines show fits of the data to constant functions.

349 those at room temperature. These measurements were performed with the HPK 50D-
 350 PIX sensors mounted on the FNAL 4-channel board. The sensor was biased at the same
 351 voltage of -250 V for all temperature scenarios. The HPK 50D gain at this bias voltage
 352 and at $+20^{\circ}\text{C}$ was measured to be 15, while at -20°C and the same bias voltage it was
 353 measured to be 25.

354 The distribution of the signal MPV across the sensor surface is shown in Fig. 15. We
 355 observe that the signal MPV increases by more than a factor of two when the temperature
 356 is reduced from $+20^{\circ}\text{C}$ to -20°C . While the MPV uniformity across the two channels
 357 are within 2% of each other at room temperature, at lower temperatures one of the pixels
 358 shows a difference of about 5% with respect to its neighboring pixel. A more detailed
 359 study is needed to understand whether this difference is due to non-uniform temperature
 360 distribution across the sensor array or due to differences in the signal response between
 361 different pixel sensors at colder temperatures.

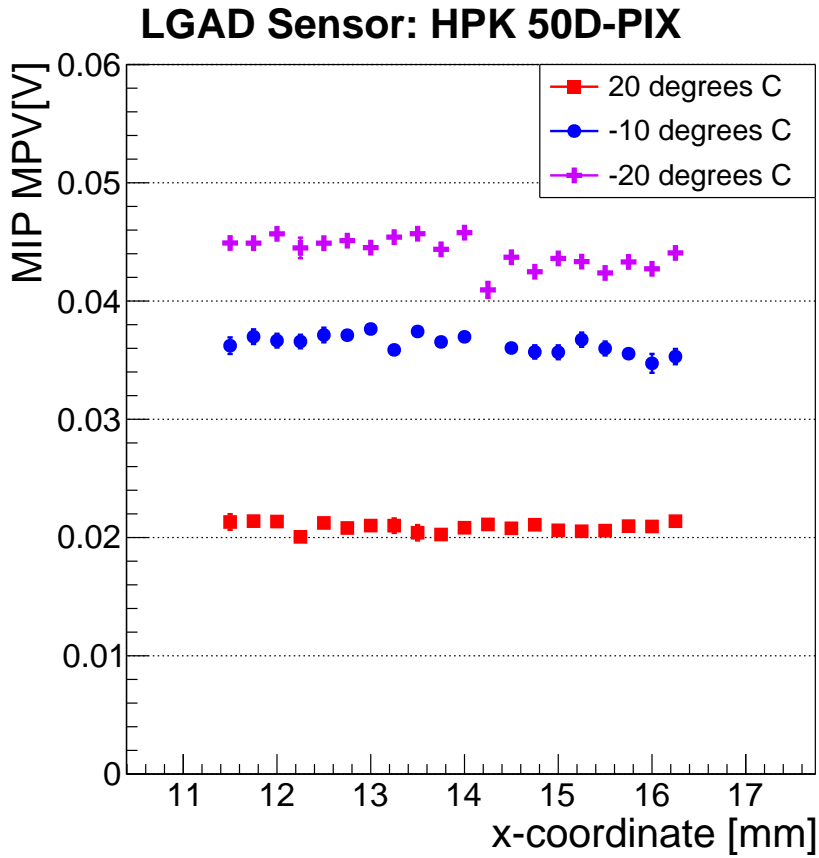


Figure 15: Temperature dependence of the signal amplitude MPV uniformity across the X-axis of the HPK 50D-PIX sensors mounted on the FNAL board. The scan of pixels 1 and 2 along the X-axis is shown, and pixel numbering scheme is defined in Fig. 3. The HPK sensor is biased at -250 V.

362 The distribution of the Δt between the reference timestamp and the timestamp from
 20

363 the HPK 50D-PIX sensor is shown in Fig. 16. We observe no significant changes in the
364 behavior of the Δt as the temperature varies.

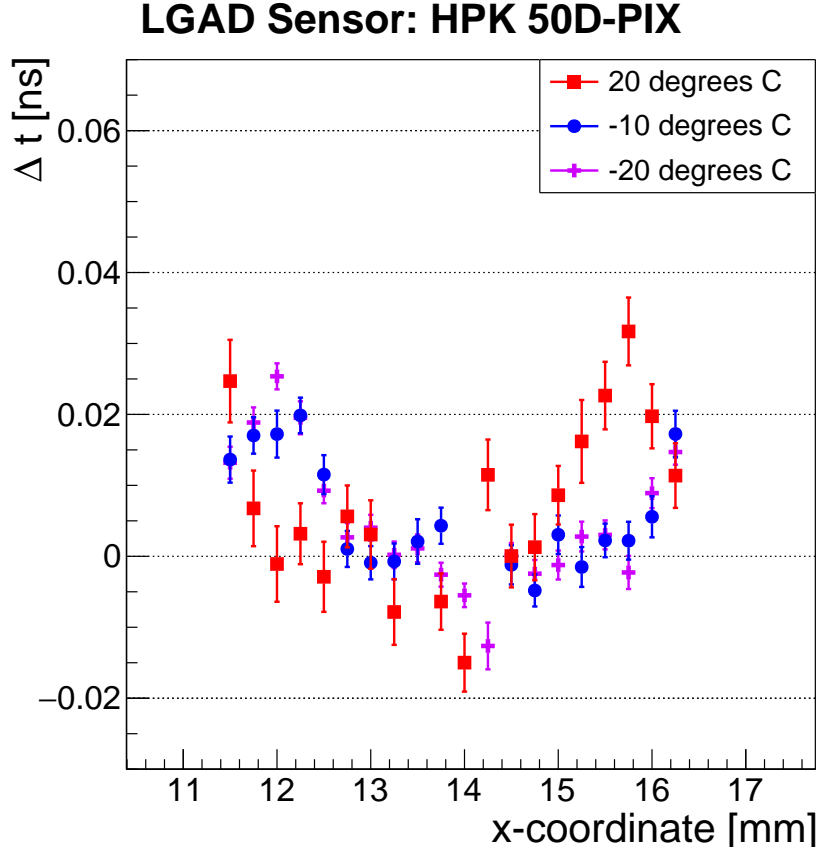


Figure 16: Temperature dependance of the Δt uniformity across the X-axis of the HPK 50D-PIX sensors mounted on the FNAL board. The scan of pixels 1 and 2 along the X-axis is shown, and pixel numbering scheme is defined in Fig. 3. The HPK sensor is biased at -250 V.

365 The time resolution measured for the HPK 50D-PIX sensor is shown in Fig. 17. We
366 observe a significant improvement in the time resolution as the temperature is lowered
367 from $+20^{\circ}\text{C}$ to -20°C degrees. As the temperature is lowered, the signal-to-noise ratio
368 improves as the gain of the LGAD sensor increases. Generally, the electronic noise may
369 also decrease as the temperature is lowered, but in our case it was observed to remain
370 relatively constant at 1.2 mV for both $+20$ and -20°C . Therefore the improvement comes
371 mainly from the increase in the signal gain. The time resolution was measured to improve
372 from around $55\text{-}60$ ps at the room temperature, down to $35\text{-}40$ ps at -20°C . It is worth
373 noting that time resolution around 35 ps with pixels of area 9 mm^2 is a promising result
374 for cost-effective implementation in LHC experiments.

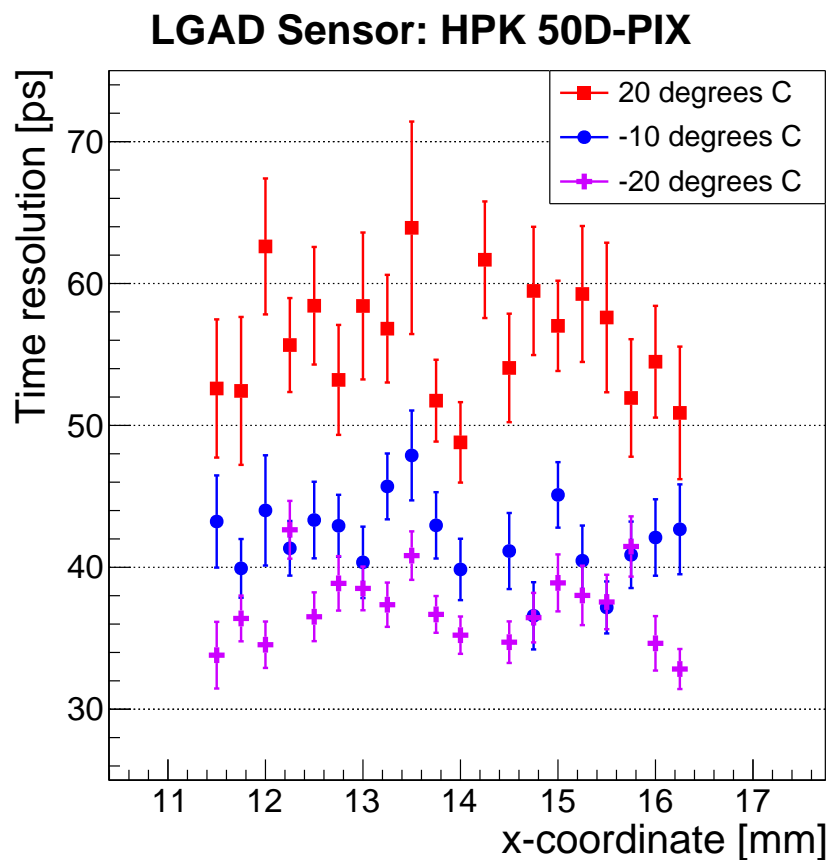


Figure 17: Temperature dependance of the time resolution uniformity across the X-axis of the HPK 50D-PIX sensors mounted on the FNAL board. The scan of pixels 1 and 2 along the X-axis is shown. The pixel numbering scheme is defined in Fig. 3. The HPK sensor is biased at -250 V.

375 6.6. Radiation tolerance of the LGADs

376 In this section we present the studies of the irradiated HPK and CNM sensors, which
 377 were exposed to neutron irradiation at the Ljubljana TRIGA reactor [15]. The neutron
 378 spectrum and flux are well known and the fluence is quoted in 1 MeV equivalent neutrons
 379 per cm² ($n_{eq.}/cm^2$ or n/cm² for short). After 6×10^{14} n/cm² irradiation, the devices were
 380 annealed for 80 min at 60°C. Afterward the devices were kept at -20°C degree during
 381 storage, transportation, and test beam experiments. Effects of neutron irradiation on
 382 LGAD sensors is documented in [6], [16], and [17].

383 The two-dimensional distribution of the signal amplitudes on the surface of the irra-
 384 diated sensors are shown in Figs. 18 and 19. From the comparison with the image of the
 385 CNM sensor shown in Fig. 3 and the distribution in Fig. 18, it is clear that two distinct
 386 regions can be identified on the sensor based on the signal amplitude: the region under
 387 the aluminum metallization on the periphery of the sensor, and the region without alu-
 388 minum metallization in the center. The distribution on the right of Fig. 18 shows that
 389 at the same bias voltage the amplitude under the aluminum (periphery) is about 2.5
 390 times larger than that without aluminum (center). The amplitude scan of the irradiated
 391 HPK 50D sensor is shown on the left panel of Fig. 19, and a uniform amplitude across
 392 the sensor surface is observed, which can also be seen on the right panel of Fig. 19. In
 393 contrast to the CNM sensor, the whole surface of the active area of the HPK 50D sensor
 394 is without metallization.

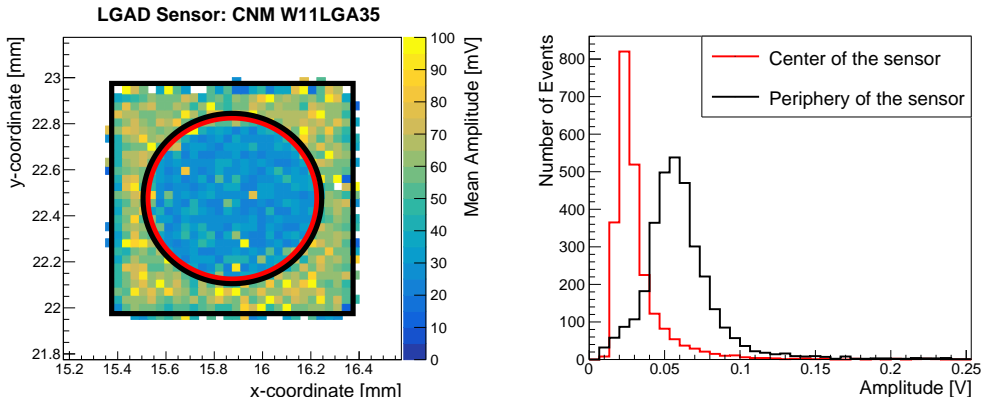


Figure 18: (Left) The map of the amplitude distribution on the irradiated CNM W11LGA35 sensor across X and Y coordinates. Two distinct regions on the sensor surface can be identified according to the amplitude distribution: the center of the sensor (area within the red circle), and the periphery of the sensor (area between the black circle and black square). (Right) Amplitude distribution in the two areas of the irradiated CNM W11LGA35 sensor. The sensor was irradiated to 6×10^{14} n/cm². Measurements were performed at -20°C.

395 Measurements of the particle detection efficiency are shown in Fig. 20. These mea-
 396 surements were performed with the HPK sensor biased at -600 V, and the CNM sensor
 397 biased at -400 V. We observe a flat 100% efficiency across the whole HPK sensor area,
 398 and the efficiency of the CNM sensor is also very close to 100%. As with the pixelated
 399 array sensors, a clear drop in efficiency is observed near the edges of the active area.

400 The distribution of MPV of signal amplitudes across the sensor area is shown in

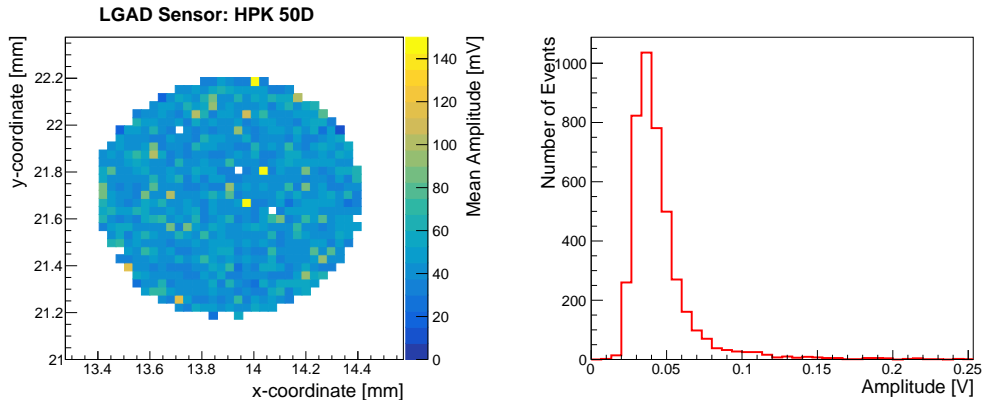


Figure 19: (Left) The map of the amplitude distribution on the irradiated HPK 50D sensor across X and Y coordinates. (Right) Signal amplitude distribution for the irradiated HPK 50D sensor. The sensor was irradiated to 6×10^{14} n/cm². Measurements were performed at -20°C .

401 Fig. 21, where the MPV is extracted as described in Sec. 6.1. Measurements were per-
 402 formed at two bias voltage values for both sensors: -600 and -635 V for HPK (gain
 403 equal to 19 and 29, respectively), and -400 and -420 V for CNM sensors (gain equal to
 404 14 and 15, respectively). A uniform signal amplitude is observed across the HPK sensor,
 405 while for the CNM sensor the amplitude varies across the sensor surface, as observed also
 406 in Fig. 18.

407 The distribution of the Δt between the reference timestamp and the timestamps of the
 408 signals from the irradiated HPK and CNM sensors are shown in Fig. 22. Measurements
 409 at both bias voltage values are presented. We measured a uniform distribution of the
 410 Δt values across the HPK sensor. The CNM sensor exhibits a non-uniformity across the
 411 sensor surface, where the signals from the central, non-metallized area arrive about 10 ps
 412 earlier than those from the peripheral, metallized area.

413 Distributions of the time resolution across the surface of the irradiated sensors are
 414 shown in Fig. 23. The time resolution measured with the HPK sensor improves slightly
 415 with the increase of the bias voltage, and shows a uniform distribution across the sensor
 416 surface. In contrast, the CNM sensor shows a non-uniform distribution of time resolution,
 417 which is a consequence of the variations of the signal amplitude across the sensor. We
 418 observe that while the signal amplitudes increases a bit, the RMS of the noise also
 419 increases from about 5.5 mV to 10 mV. As a consequence, we observe a small degradation
 420 of the time resolution for the CNM sensor as the bias voltage is increased.

421 7. Conclusion

422 In a beam test at FNAL with tracking information, we compared the performance
 423 of LGAD produced by CNM Barcelona and HPK Hamamatsu. Single pads of diameter
 424 1 mm and 2×2 arrays of square pixels of 3 mm were used. Sensors with thicknesses of
 425 about 50 and 80 μm were studied. The uniformity of the sensor response in pulse height,
 426 efficiency, and timing resolution were studied. Four different readout boards were used
 427 in these studies. The uniformity of the sensor response in pulse height before irradiation

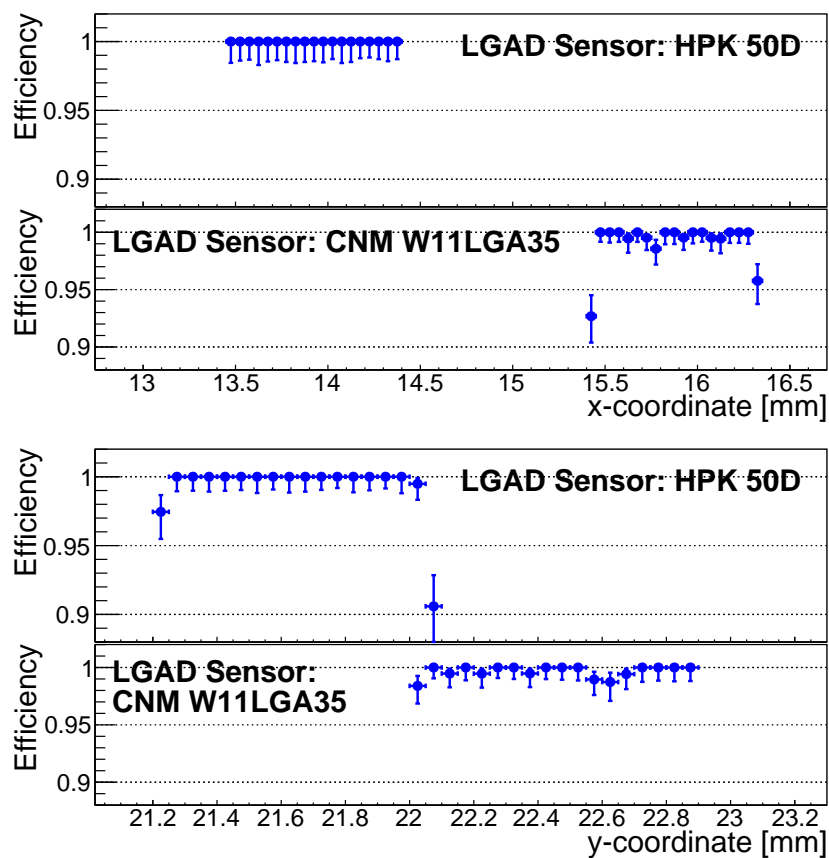


Figure 20: Efficiency measurements across the X-axis (top) and Y-axes (bottom) of the HPK 50D and CNM W11LGA35 irradiated sensors. Both sensors were irradiated to $6 \times 10^{14} \text{ n/cm}^2$. Measurements were performed at -20°C .

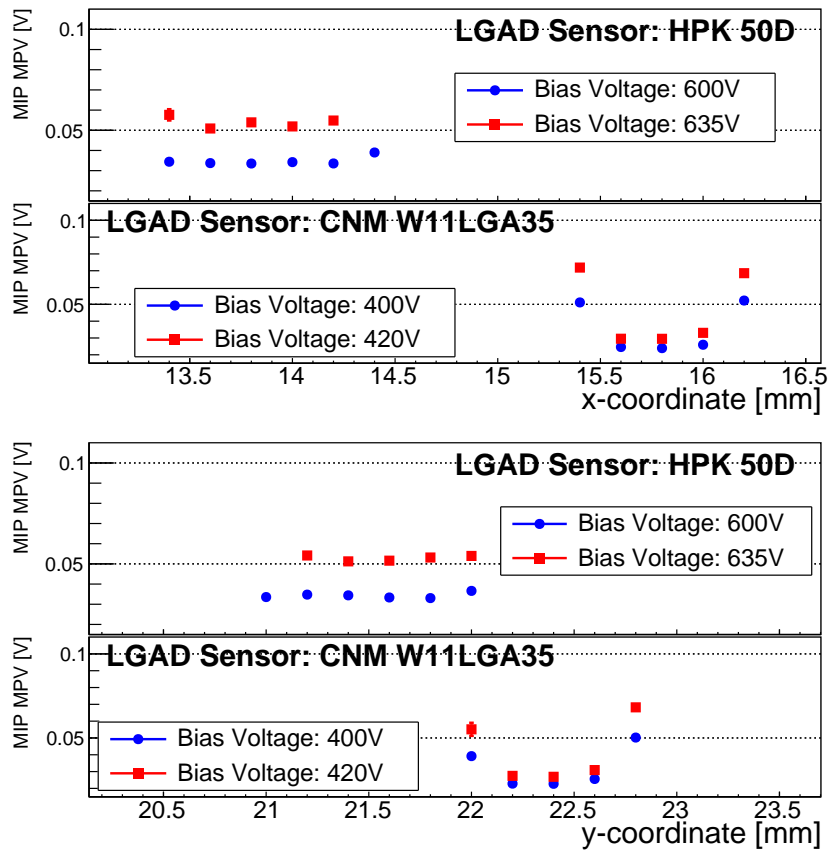


Figure 21: Signal amplitude MPV measurement across the X-axis (top) and Y-axes (bottom) of the HPK 50D and CNM W11LGA35 irradiated sensors. Both sensors were irradiated to $6 \times 10^{14} \text{ n/cm}^2$. Measurements were performed at -20°C .

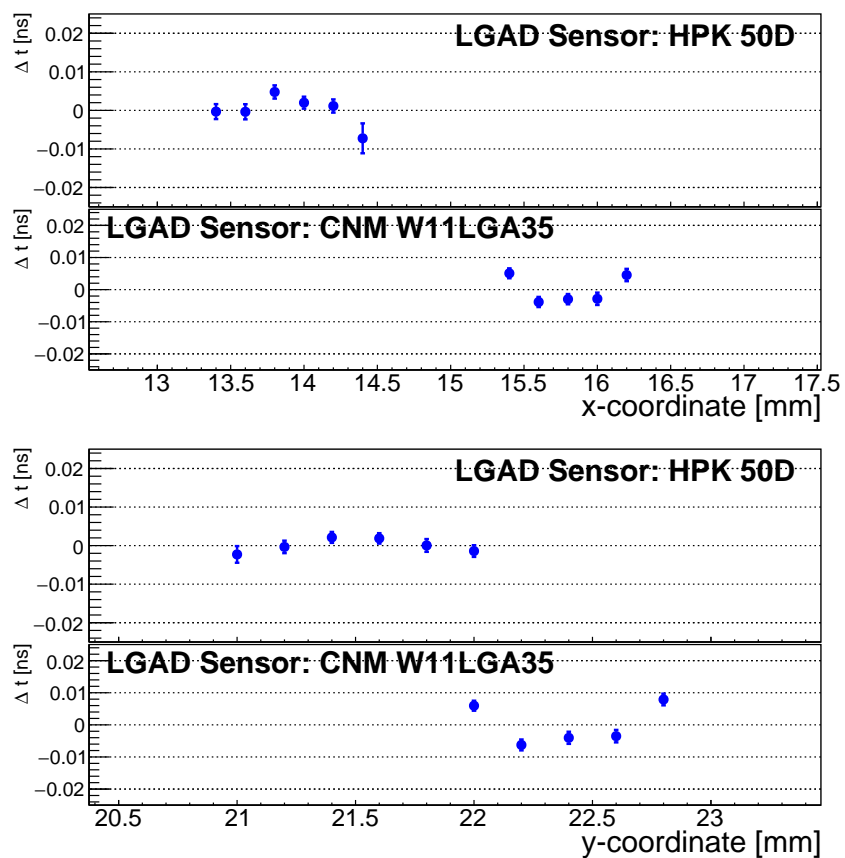


Figure 22: Δt measurements across the X-axis (top) and Y-axes (bottom) of the HPK 50D and CNM W11LGA35 irradiated sensors. Both sensors were irradiated to 6×10^{14} n/cm². Measurements were performed at -20°C .

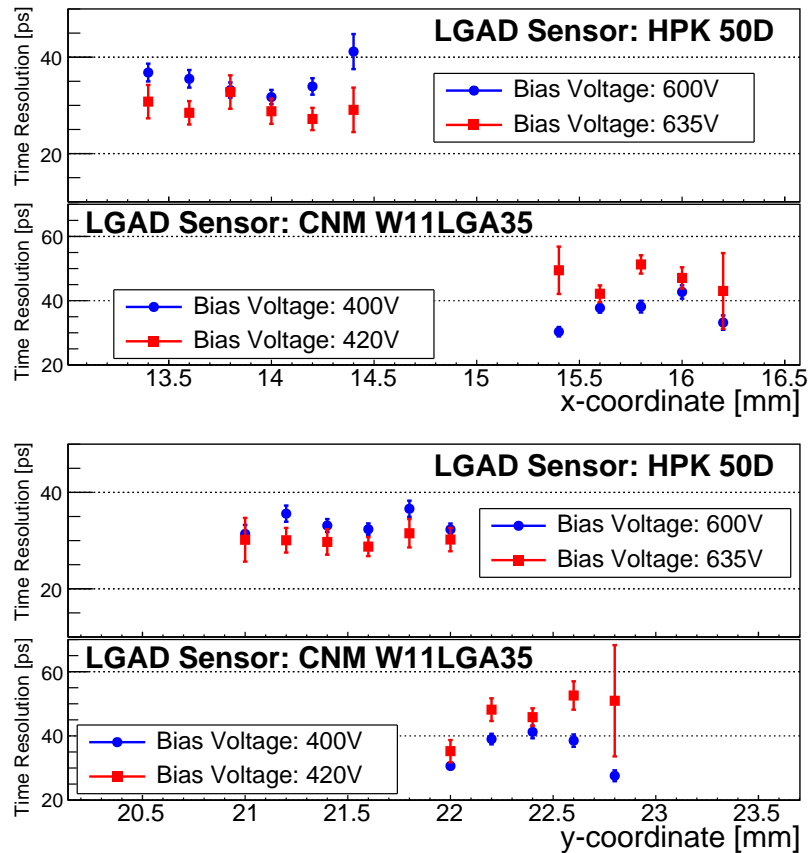


Figure 23: Time resolution measurements across the X-axis (top) and Y-axes (bottom) of the HPK 50D and CNM W11LGA35 irradiated sensors. Both sensors were irradiated to $6 \times 10^{14} \text{ n/cm}^2$. Measurements were performed at -20°C .

428 was found to have a 2% spread. The efficiency and timing resolution before irradiation
429 were found to be 100% and 30-40 ps, respectively. The “non-response” region between
430 pixels was measured to be about $70\text{ }\mu\text{m}$ for CNM sensors and $110\text{ }\mu\text{m}$ for HPK sensors. A
431 small timing shift across the HPK sensor of the order 20–30 ps¹ can be explained by the
432 observed change in pulse shape when comparing metallized and non-metallized sensor
433 areas. Uniform signal detection efficiency of 100% is observed on all sensors, both before
434 and after irradiation.

435 For an un-irradiated $50\text{ }\mu\text{m}$ thick LGADs with 3 mm pads we find the following timing
436 results:

- 437 • at a temperature of $+20^\circ\text{C}$, the timing resolution ranges from 40 ps to 50 ps
438 depending on the readout board.
- 439 • cooling the LGAD, while keeping the bias voltage the same at -250 V , improves
440 the timing resolution from 55 ps at $+20^\circ\text{C}$ to 43 ps at -10°C to 36 ps at -20°C .

441 After a neutron fluence of $6 \times 10^{14}\text{ n/cm}^2$, the single pad CNM sensor exhibits a
442 large gain variation of a factor 2.5 when comparing metallized and non-metallized sensor
443 areas. For an $50\text{ }\mu\text{m}$ thick LGAD with 1 mm pads irradiated $6 \times 10^{14}\text{ n/cm}^2$ we find the
444 following timing results when operated at -20°C :

- 445 • for the HPK LGAD the highest bias voltage reached is -635 V and the correspond-
446 ing timing resolution is 30 ps;
- 447 • for the CNM LGAD the highest bias voltage reached is -420 V and the correspond-
448 ing timing resolution is 30 ps for the metallized area and 40 ps for the non-metallized
449 area.

450 Acknowledgement

451 We thank the FTBF personnel and Fermilab accelerator’s team for very good beam
452 conditions during our test beam time. We also appreciate the technical support of the
453 Fermilab SiDet department for the rapid production of wire-bonded and packaged LGAD
454 assemblies. We would like to thank Alan Prosser and Ryan Rivera for their critical help
455 in setting up the DAQ and trigger chain. We thank Ned Spencer, Max Wilder, and Forest
456 McKinney-Martinez for their technical assistance, and the CNM and HPK manufacturing
457 team. We acknowledge the help of V. Cindro and I. Mandic with the neutron irradiations.

458 This document was prepared using the resources of the Fermi National Accelerator
459 Laboratory (Fermilab), a U.S. Department of Energy, Office of Science, HEP User Facility.
460 Fermilab is managed by Fermi Research Alliance, LLC (FRA), acting under Contract
461 No. DE-AC02-07CH11359. Part of this work was performed within the framework of
462 the CERN RD50 collaboration.

463 This work was supported by the Fermilab LDRD 2017.027; by the United States
464 Department of Energy grant DE-FG02-04ER41286; by the California Institute of Tech-
465 nology High Energy Physics under Contract DE-SC0011925; by the European Union’s
466 Horizon 2020 Research and Innovation funding program, under Grant Agreement no.
467 654168 (AIDA-2020) and Grant Agreement no. 669529 (ERC UFSD669529); by the
468 Italian Ministero degli Affari Esteri and INFN Gruppo V; and by the Spanish Min-
469 istry of Economy, Industry and Competitiveness through the Particle Physics National

470 Program (ref. FPA2014-55295-C3-2-R and FPA2015-69260-C3-3-R) co-financed with
471 FEDER funds.

472 References

- 473 [1] A. Apresyan, G. Bolla, A. Bornheim, H. Kim, S. Los, C. Pena, E. Ramberg, A. Ronzhin, M. Spiropulu, and S. Xie, "Test beam studies of silicon timing for use in calorimetry," *Nuclear Instruments and Methods in Physics Research Section A: Accelerators, Spectrometers, Detectors and Associated Equipment*, vol. 825, pp. 62 – 68, 2016.
- 474 [2] A. Apresyan, "Investigation of Fast Timing Capabilities of Silicon Sensors for the CMS High Granularity Calorimeter at HL-LHC," in *Proceedings, 2016 IEEE Nuclear Science Symposium and Medical Imaging Conference (NSS/MIC 2016)*, Oct 2016. <http://2016.nss-mic.org/index.php>.
- 475 [3] N. Akchurin, V. Ciriolo, E. Currs, J. Damgov, M. Fernandez, C. Gallrapp, L. Gray, A. Junkes, M. Mannelli, K. M. Kwok, P. Meridiani, M. Moll, S. Nourbakhsh, S. Pigazzini, C. Scharf, P. Silva, G. Steinbrueck, T. T. de Fatis, and I. Vila, "On the timing performance of thin planar silicon sensors," *Nuclear Instruments and Methods in Physics Research Section A: Accelerators, Spectrometers, Detectors and Associated Equipment*, vol. 859, pp. 31 – 36, 2017.
- 476 [4] N. Cartiglia *et al.*, "Beam test results of a 16 ps timing system based on ultra-fast silicon detectors," *Nucl. Instrum. Meth. A*, vol. 850, pp. 83 – 88, 2017.
- 477 [5] G. Pellegrini, P. Fernández-Martínez, M. Baselga, C. Fleta, D. Flores, V. Greco, S. Hidalgo, I. Mandić, G. Kramberger, D. Quirion, and M. Ullan, "Technology developments and first measurements of Low Gain Avalanche Detectors (LGAD) for high energy physics applications," *Nuclear Instruments and Methods in Physics Research Section A: Accelerators, Spectrometers, Detectors and Associated Equipment*, vol. 765, pp. 12 – 16, 2014. HSTD-9 2013 - Proceedings of the 9th International.
- 478 [6] Z. Galloway *et al.*, "Properties of HPK UFSD after neutron irradiation up to 6e15 n/cm²," 2017. arXiv/1707.04961 [physics.ins-det].
- 479 [7] S. Kwan, C. Lei, D. Menasce, L. Moroni, J. Ngadiuba, A. Prosser, R. Rivera, S. Terzo, M. Turqueti, L. Uplegger, L. Vigani, and M. E. Dinardo, "The pixel tracking telescope at the fermilab test beam facility," *Nuclear Instruments and Methods in Physics Research Section A: Accelerators, Spectrometers, Detectors and Associated Equipment*, vol. 811, pp. 162 – 169, 2016.
- 480 [8] D. Anderson, A. Apresyan, A. Bornheim, J. Duarte, C. Pena, A. Ronzhin, M. Spiropulu, J. Trevor, and S. Xie, "On Timing Properties of LYSO-Based Calorimeters," *Nucl. Instrum. Meth. A*, vol. 794, pp. 7–14, 2015.
- 481 [9] A. Ronzhin, S. Los, E. Ramberg, M. Spiropulu, A. Apresyan, S. Xie, H. Kim, and A. Zatserklyaniy, "Development of a new fast shower maximum detector based on microchannel plates photomultipliers (MCP-PMT) as an active element," *Nucl. Instrum. Meth. A*, vol. 759, pp. 65 – 73, 2014.
- 482 [10] A. Ronzhin, S. Los, E. Ramberg, A. Apresyan, S. Xie, M. Spiropulu, and H. Kim, "Study of the timing performance of micro-channel plate photomultiplier for use as an active layer in a shower maximum detector," *Nucl. Instrum. Meth. A*, vol. 795, pp. 288 – 292, 2015.
- 483 [11] A. Ronzhin, S. Los, E. Ramberg, A. Apresyan, S. Xie, M. Spiropulu, and H. Kim, "Direct tests of micro channel plates as the active element of a new shower maximum detector," *Nucl. Instrum. Meth. A*, vol. 795, pp. 52 – 57, 2015.
- 484 [12] <http://www.caen.it/cssite/CaenProd.jsp?parent=11&idmod=661>.
- 485 [13] H. Kim, C.-T. Chen, N. Eclov, A. Ronzhin, P. Murat, E. Ramberg, S. Los, W. Moses, W.-S. Choong, and C.-M. Kao, "A new time calibration method for switched-capacitor-array-based waveform samplers," *Nucl. Instrum. Meth. A*, vol. 767, pp. 67 – 74, 2014.
- 486 [14] M. Carulla *et al.*, "First 50 m thick LGAD fabrication at CNM." <https://agenda.infn.it/getFile.py/access?contribId=20&sessionId=8&resId=0&materialId=slides&confId=11109>, 2016. 28th RD50 Workshop, Torino.
- 487 [15] L. Snoj, G. Žerovnik, and A. Trkov, "Computational analysis of irradiation facilities at the jsi triga reactor," *Applied Radiation and Isotopes*, vol. 70, no. 3, pp. 483 – 488, 2012.
- 488 [16] H. F.-W. Sadrozinski, A. Seiden, and N. Cartiglia, "4d tracking with ultra-fast silicon detectors," *Reports on Progress in Physics*, vol. 81, no. 2, p. 026101, 2018.
- 489 [17] G. Kramberger, M. Baselga, V. Cindro, P. Fernandez-Martinez, D. Flores, Z. Galloway, A. Goriek, V. Greco, S. Hidalgo, V. Fadeyev, I. Mandi, M. Miku, D. Quirion, G. Pellegrini, H.-W. Sadrozinski, A. Studen, and M. Zavrtanik, "Radiation effects in low gain avalanche detectors after hadron irradiations," *Journal of Instrumentation*, vol. 10, no. 07, p. P07006, 2015.